# Chapter 2
# Controlling the Nanostructure of Electrospun Polymeric Fibers

**Israel Greenfeld and Eyal Zussman**

**Abstract** The high strain rate extensional flow of a semi-dilute polymer solution can cause substantial stretching and disentanglement of the polymer network. In this study, we conducted a theoretical and experimental investigation of the effects of electrospinning, a flow governed by high strain rate and rapid evaporation, on the polymer matrix of the resulting nanofibers. Modeling of the dynamic evolution of the entangled polymer network in an electrospinning jet predicted substantial longitudinal stretching and radial contraction of the network, a transformation from an equilibrium state to an almost fully-stretched state. This prediction was verified by X-ray phase-contrast imaging of electrospinning jets, which revealed a noticeable increase in polymer concentration at the jet center, within a short distance from the jet start. Additionally, polymer entanglement loss in consequence of stretching was evidenced in jet fragmentation and appearance of short nanofibers, affecting the entanglements density and molecular orientation of as-spun fibers. The stretching model was expanded to semi-flexible conjugated polymer chains, and scanning near field optical microscopy of electrospun nanofibers of such optically active polymers revealed that the network's dense elongated conformation effectively remains after jet solidification. By tuning the electrospinning conditions, the unique size-dependent properties of nanofibers can be controlled and improved, potentially leading to novel applications in engineering and life sciences.

I. Greenfeld (✉)
Department of Mechanical Engineering, Technion – Israel Institute of Technology,
Haifa 32000, Israel

Department of Materials and Interfaces, Weizmann Institute of Science, Rehovot 76100, Israel
e-mail: green_is@netvision.net.il

E. Zussman
Department of Mechanical Engineering, Technion – Israel Institute of Technology,
Haifa 32000, Israel

35

## 2.1 Introduction

Electrospinning has attracted considerable attention in the past decade as an accessible and scalable process for creating nanostructures. An electrospinning jet is created when a polymer solution is drawn from a capillary and stretched by the force of a strong electric field (Fig. 2.1), producing very thin fibers – nanofibers – of diameters ranging typically from 50 to 1,000 nm [1–4].

Electrospun polymeric nanofibers exhibit unique properties. For example, below a certain crossover diameter, dependent on the polymer molar mass, the nanofiber elastic moduli begin to rise sharply [5–11]. Similarly, in optically active polymers, the effective conjugation length of chromophores increases as a result of electrospinning, and their optical absorption and emission become polarized along the fiber axis [12, 13]. Better understanding of the mechanisms behind these phenomena can help improving the mechanical, electrical and optical properties of nanofibers, and can lead to novel applications in engineering and life sciences.

Electrospinning is an extensional flow characterized by high strain rates of order $10^3$ $s^{-1}$ [14–20]. Such stretching can potentially increase the structural order within as-spun nanofibers and enhance their mechanical properties such as elastic modulus
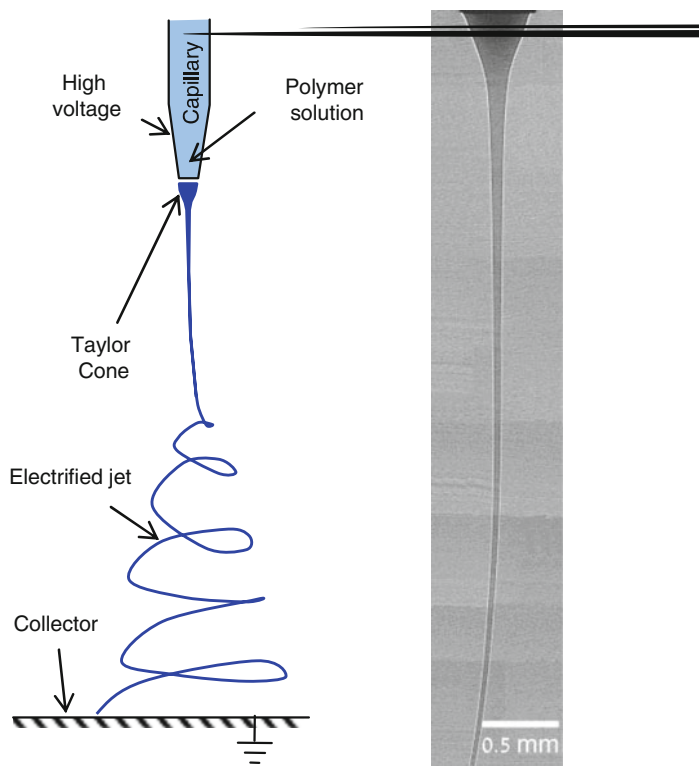


**Fig. 2.1** (**a**) Schematics of the electrospinning setup and process. (**b**) Example of the rectilinear section of a jet (~5 mm length), imaged by fast phase-contrast X-ray. Conditions: molar mass 600 kDa PEO, concentration 5 wt% in water, electric field 0.6 kV/cm, flow rate 3.2 mL/h, electric field gap 6.5 cm
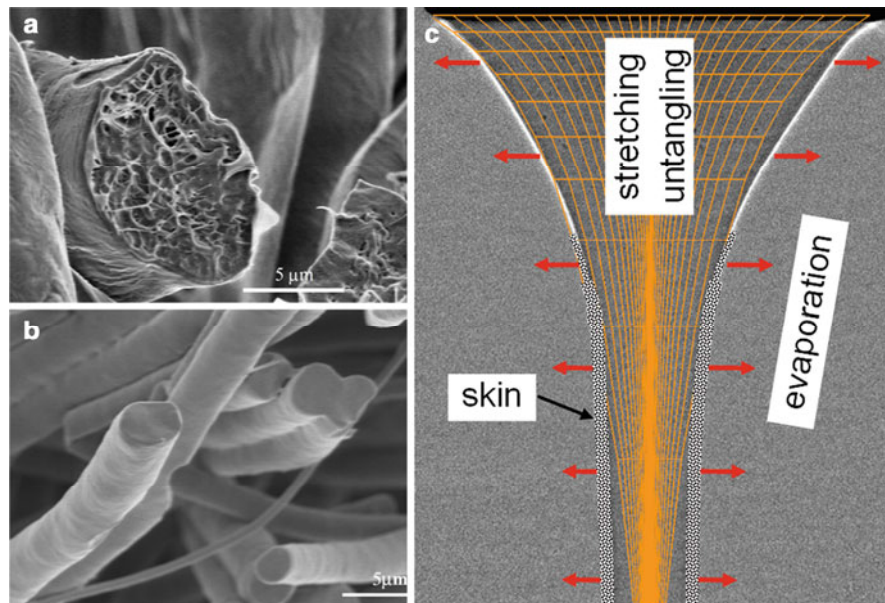
**Fig. 2.2** Stretching and evaporation during electrospinning. (**a**)(**b**) SEM images of electrospun nanofibers of 10 wt% PCL with molar mass 80 kDa, dissolved in DCM/DMF (75:25 wt%), under an electric field of 0.63 kV/cm. (**a**) High flow rate of 20 ml/h resulting in heterogeneous fibers. (**b**) Low flow rate of 3 ml/h resulting in homogeneous fibers. (**c**) Illustration of stretching, untangling and evaporation effects [21]

and strength [5, 8–11, 21, 22]. At the same time, rapid solvent evaporation during electrospinning can lead to increased polymer concentrations at the jet boundary [23–26], sometimes forming a solid skin and a heterogeneous and porous structure [21, 25, 27]. The simultaneous effects of stretching and evaporation are illustrated in Fig. 2.2. Hence, study of electrospinning polymer solution jets, and specifically of the evolution of the polymer entangled network during electrospinning, is of interest in clarifying the microstructure of as-spun nanofibers.

The presentation in this text is broadly based on [12, 13, 21, 28–30]. In this study, modeling and random walk simulations of the dynamic evolution of the entangled polymer network in an electrospinning jet predicted substantial longitudinal stretching and radial contraction of the network, a transformation from an equilibrium state to an almost fully-stretched state [21]. This prediction was verified by fast X-ray phase-contrast imaging of electrospinning jets, which revealed a noticeable increase in polymer concentration at the jet center, as well as a concentration crossover within a short distance from the jet start [28].

Furthermore, modeling showed that polymer entanglement loss, due to network stretching under very high strain rates, reduces the fiber diameter and enhances the homogeneity and alignment of the nanostructure. This effect was evidenced by jet fragmentation and appearance of short nanofibers during extreme electrospinning conditions [29].

To examine whether the compact stretched network conformation remains after jet solidification, we electrospun MEH-PPV nanofibers. This conjugated semi-flexible optically active polymer has high absorption in the visible waveband, and is shown by the simulation to have a fast response to stretching owing to its long rigid segments. Scanning near field optical microscopy (SNOM) of such nanofibers at nano-resolution revealed a dense core with an increased elastic modulus [12], as well as an axial molecular alignment that affects the polarization of optical absorption and emission, which can be tuned [13].

The following sections expand on these findings and explain their meaning in the context of the question whether we can control and tune the nanostructure of electrospun fibers for the benefit of improving their properties.

## 2.2  Polymer Dynamics During Electrospinning

The flow of an electrospinning jet is viscoelastic and consists of axial and radial velocity components (Fig. 2.3). Analysis of electrically driven fluid jets has shown that the axial jet velocity $v_z$ reaches an asymptotic regime sufficiently far from the needle orifice, which can be described by a power law of the distance $z$:
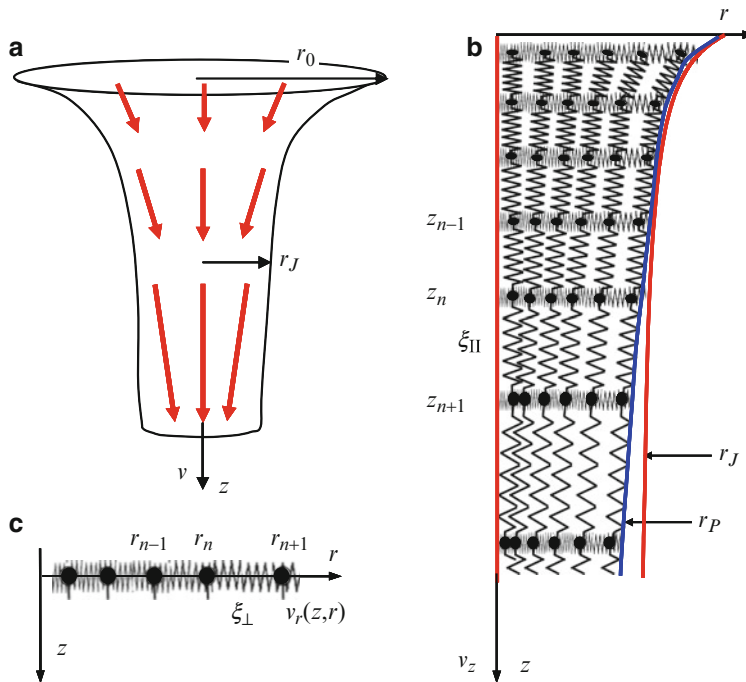


**Fig. 2.3** (**a**) Illustration of the flow of an electrospinning jet. (**b**) Definition of an effective 1D beads-and-springs system in the axial direction and (**c**) the radial direction [21]

$$\frac{v_z}{v_0} \approx k^2 \left(\frac{z}{r_0}\right)^{2\beta},$$

(2.1)

where $\beta$ varies between 1/4 and 1 [31–35], $r_0$ is the jet initial radius, and $v_0$ is the initial velocity. Assuming volume conservation, the jet local radius $r_J/r_0 \cong (v_z/v_0)^{-1/2}$ and the radial velocity $v_r$ can be derived.

We can obtain a rough approximation of the dimensionless parameter $k$ by using a simple scaling approach: the velocity gradient scales as $\nabla v \sim v_0 k^2/r_0^2$; the upper bound for the electric charge surface density, assuming static conditions, scales as $s \sim \sigma E$, where $\sigma$ is the solution's electric conductance and $E$ is the electric field intensity; the electric shear stress is therefore $\tau_t \approx sE \sim \sigma E^2$, producing a velocity gradient $\nabla v \approx \tau_t/\eta \sim \sigma E^2 \eta^{-1}$, where $\eta$ is the solution viscosity; hence, $k \sim \nabla v^{1/2} v_0^{-1/2} r_0$, or $k \sim r_0^1 \sigma^{1/2} \eta^{-1/2} v_0^{-1/2} E^1$. A more accurate calculation yields $k \cong r_0^{2/3} v_0^{-2/3} \sigma^{1/4} \eta^{-5/12} E^{5/6} \sim 1$ [35].

Polymer chains dissolved in a sufficiently concentrated semi-dilute solution create an entangled network (Fig. 2.3b), a prerequisite for the polymer solution successful spinability. A chain section between two subsequent entanglements is a strand, or a subchain, consisting of $N_s$ rigid segments (Kuhn monomers), each of size $b \sim 1_{nm}$.

Given the solution concentration $\phi$ (in terms of the polymer volume fraction), the network mesh size (i.e., average subchain length) is given by $\xi_0 \approx b\phi^{-1} \approx b N_s^{1/2}$ for ideal chains, allowing the modeling of the network as a 3D beads and springs lattice, where each bead represents the mass $m$ and size $\xi_{eff}$ of a subchain, and the springs represent the linear entropic elasticity $T/\xi_0^2$ ($T$ is the temperature in units of the Boltzmann constant $k_B$) of the subchains connected to each bead. Using the known rheology of electrified jets, the hydrodynamic force acting on a subchain can be defined, and the dynamics of the network can be described by difference-differential equations [21]:

$$m\frac{d^2z_n}{dt^2} = \xi_{eff}\eta\left[v_z(z_n) - \frac{dz_n}{dt}\right] + \frac{T}{\xi_0^2}\{[z_{n+1} - z_n - \xi_0] - [z_n - z_{n-1} - \xi_0]\}$$
$$\xi_{eff}\eta v_r(r_n) + \frac{T}{\xi_0^2}\{[r_{n+1} - r_n - \xi_\perp] - [r_n - r_{n-1} - \xi_\perp]\} = 0.$$

(2.2)

The solution of this equation in the axial direction $z$, depicted in Fig. 2.4, predicts an affine stretching of the network

$$\frac{\xi_\parallel(z)}{\xi_0} \approx \frac{v_z/v_0}{1 - \frac{1}{\alpha}d(v_z/v_0)/d(z/r_0)} \approx \frac{v_z(z)}{v_0},$$

(2.3)

where the dimensionless parameter $\alpha \gg 1$ [21].

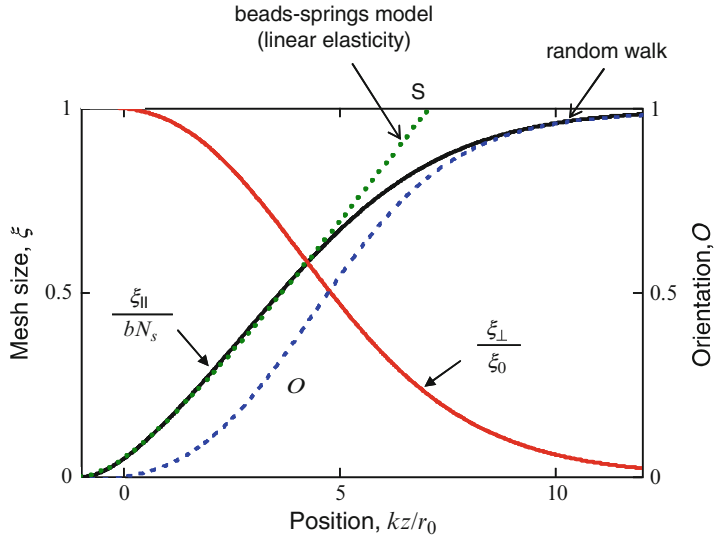**Fig. 2.4** Universal plot of the polymer network conformation. Relative axial stretching, $\xi_{\parallel}/bN_s$, radial contraction, $\xi_{\perp}/\xi_0$, and molecular orientation $O$, vs. the normalized axial position, $kz/r_0$. $bN_s$ is the length of a fully extended subchain. The results were obtained by random walk simulation and theoretical modeling. The point S indicates the criterion for 'full' network extension [21]

**Fig. 2.5** Forces acting on a subchain: external forces act at chain ends, and a hydrodynamic force acts on each monomer
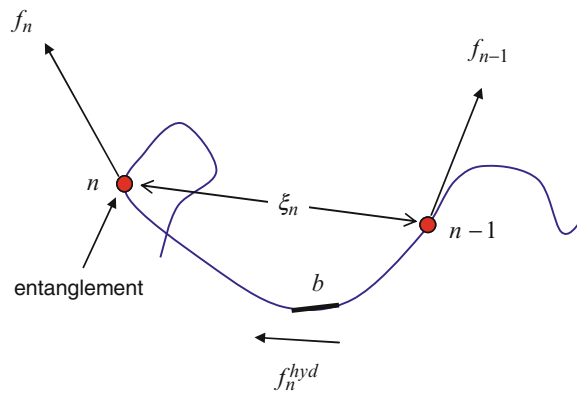


The dynamic conformation of subchains can be described by a random walk simulation, where each step represents a single monomer. The probability to step in a specific direction is determined by an effective potential, which arises from the external forces acting at the subchain ends, which propagate along the subchain, and the local hydrodynamic force acting directly on monomers (Fig. 2.5).

For a given force vector $F$ acting on a monomer [normalized as $f = Fb/(k_BT)$], the probabilities for a random walk step are

$$P_x^\pm = \frac{\exp(\pm f_x)}{2\sum_x \cosh(f_x)}, \quad x = z, \rho, \varphi, \tag{2.4}$$

in each of the 6 Cartesian directions [21]. The monomer forces in the radial and axial directions are given by

$$f_\rho \cong f_0 \approx 3b/\xi_0 \approx 3\phi$$
$$f_z \cong f_0 + \sum_{i=1}^n f_i^{hyd} \cong f_0 + \tau_0(v_z - v_0)/b, \tag{2.5}$$

where $f_0$ is caused by an effective stretching force acting on subchains in a network at rest, and $\tau_0 \approx \eta_s b^3/(k_B T)$ is the monomer relaxation time given the solvent viscosity $\eta_s$. The hydrodynamic force in the radial direction is small compared to the force in the axial direction, since $f_\rho/f_z \cong v_\rho/v_z \approx \rho/z << 1$, and was therefore neglected.

Since the dominant force acts at the subchain ends, the stepping probabilities remain uniform along the subchain, and the axial stretching and radial contraction can be written using (2.4) and (2.5) [21]:

$$\xi_\|/\xi_{\max} \cong \sinh(f_z)/Q$$
$$\xi_\perp/\xi_{\max} \cong \sinh(f_\rho)/Q \tag{2.6}$$
$$Q = \cosh(f_z) + 2\cosh(f_\rho).$$

Shortly after the jet start, but before the network approaches full stretching ($f < 1$), the relative longitudinal elongation of a subchain can be approximated by

$$\frac{\xi_\|}{\xi_0} \approx \frac{\xi_0 v_0 \tau_0}{3b^2}\left(\frac{v_z}{v_0}\right) \approx \frac{v_z}{v_0}, \tag{2.7}$$

as obtained by the dynamic model (2.3). The condition for affine stretching is satisfied when the prefactor $\xi_0 v_0 \tau_0/(3b^2) = 1$, in which case the vertical force simplifies to $f_z \cong 3\phi v_z/v_0$.

The simulation allows expansion of the analysis to large chain elongations with non-linear elasticity, and shows that subchains approach full extension not far (<1 mm) from the jet start (Fig. 2.4). The criterion established for such full extension [marked by point S in Fig. 2.4, using (2.3) or (2.7)] is when the jet velocity rises above its initial value by a factor equal to the inverse of the polymer volume fraction:

$$\frac{v_{zS}}{v_0} \approx \frac{\xi_{\|S}}{\xi_0} \approx \frac{bN_s}{bN_s^{1/2}} \approx N_s^{1/2} \approx \phi^{-1}, \tag{2.8}$$

which occurs at a jet radius reduction ratio of $r_0/r_S \approx N_s^{1/4} \approx \phi^{-1/2} \sim 2 \div 10$. Note that the relative velocity and radius at the stretching crossover point depend

only on the solution concentration, and are completely independent of the electrospinning materials and conditions (e.g., molar mass and electric field).

The transformation of subchains from a coil-like equilibrium state into a stretched state occurs as a continuous crossover, and no phase transition is observed, in contrast to the well-known coil stretch transition in unentangled chains described by de Gennes [36, 37]. The dominant local force on a subchain is the elastic force arising from the action of the linked subchains, whereas the local hydrodynamic forces, whose accumulation along the network gives rise to the global elastic stretching, are negligible. Theoretically, since a vertical sequence of subchains in a network is analogous to a very long chain, a network stretch transition is possible if the jet strain rate is very low; however, under such conditions, the flow will be dominated by viscosity and network relaxation rather than elasticity.

The strong increase in the longitudinal mesh size, $\xi_{\parallel}$, results in a decrease in the radial mesh size, $\xi_{\perp}$, due to redistribution of the random walk stepping probabilities (Fig. 2.4). The result is a lateral contraction of the network toward the jet center (Fig. 2.6), which is proportional to the decrease in the subchains radial mesh size.

An approximation for the decrease of the polymer network radius with respect to the jet radius is given by

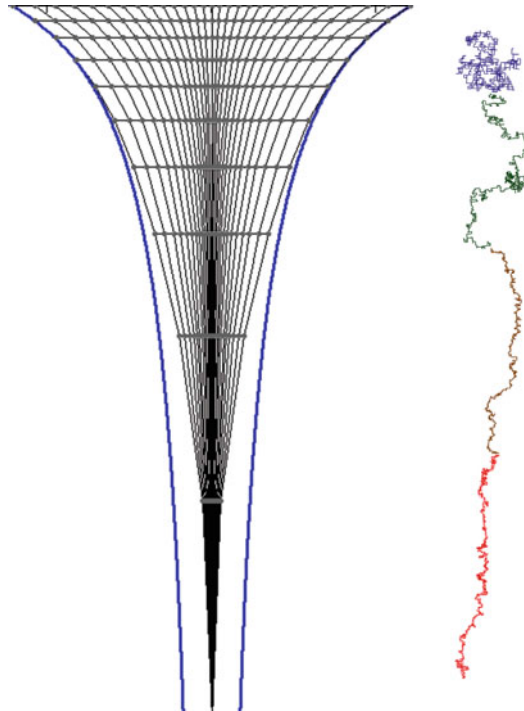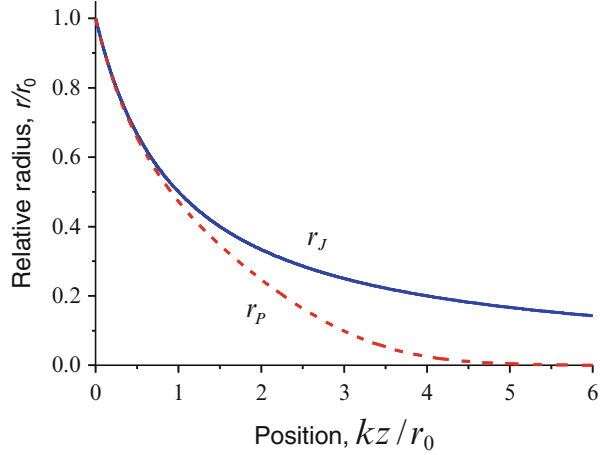$$r_P(z) \cong \frac{\xi_{\perp}(z)}{\xi_0} r_J(z) \tag{2.9}$$



**Fig. 2.6** Typical simulated conformation of a polymer network during electrospinning (*left*, diluted x800), and a vertical sequence of linked subchains (*right*, not to scale)

**Fig. 2.7** Universal plot of the simulated polymer network radius, $r_P/r_0$, vs. the normalized axial position, $kz/r_0$, compared to the jet radius $r_J/r_0$ [21]



(depicted in Fig. 2.7), showing the dominant effect of axial stretching on the radial contraction [21]. This result allows predicting a significant increase of the polymer concentration at the jet center. The concentration (in terms of the polymer volume fraction) can be calculated by $\phi_p = b^3 N_s/(\xi_\| \xi_\perp^2)$ or by

$$\phi_p = \phi \left(\frac{r_J}{r_P}\right)^2 = \phi \left(\frac{\xi_0}{\xi_\perp}\right)^2 \cong \frac{\phi}{9}\left[\cosh\left(3\phi\frac{v_z}{v_0}\right) + 2\right]^2, \qquad (2.10)$$

using (2.6) and (2.9) and the relationship $\phi \approx b/\xi_0$, where $\phi$ is the solution initial concentration. The right term assumes affine stretching by means of the vertical force $f_z \cong 3\phi v_z/v_0$. When full stretching occurs, the polymer at the jet core is fully compacted ($\phi_p \cong 1$), and the corresponding jet radius can be approximated by $r_S/r_0 \cong [3/\ln(6/\sqrt{\phi})]^{1/2}\phi^{1/2} \approx \phi^{1/2}$, the same result as in (2.8). These predictions were validated by X-ray absorption measurements of electrospinning jets, which indicated a significant increase in polymer concentration close to the jet center (see Fig. 2.12).

The validity of the network modeling is restricted to the initial stage of the jet (first few millimeters), where elastic elongation is still possible, and therefore the model does not describe the final state of the polymer matrix in electrospun nanofibers. Additional processes, such as rapid solvent evaporation and polymer entanglement loss, which can result in chain relaxation, are not accounted for in the model, and are further addressed in later sections. Nevertheless, the results strongly indicate non-equilibrium, ordered nanostructures that could remain in the nanofibers after solidification, structures which may set a new internal scale, and affect the nanofiber elasticity through confinement.

## 2.3 X-ray Imaging of Electrospinning Jets

The theoretically predicted longitudinal stretching and lateral contraction of the polymer network, as well as the additional effects of rapid evaporation, were investigated experimentally by fast X-ray, phase-contrast, high-resolution imaging of the first 10 mm of electrospinning jets, using solutions of PEO [poly(ethylene oxide)] and PMMA [poly(methyl methacrylate)]. The experimental setup is shown in Fig. 2.8.

The power law jet rheology (2.1), assumed in the theoretical model, was validated by detailed measurements of the jet profile under a wide range of electrospinning conditions and polymer solutions, demonstrating that the jet diameter narrows faster under higher electric fields, lower flow rates, and lower polymer concentrations (Fig. 2.9). The measurements validate the theoretical expression of the parameter $k$ defined in (2.1).

Comparison of velocity measurements obtained by particle tracing velocimetry to estimates based on volume conservation assumption, showed an abrupt deviation 1–2 mm from the jet start, a possible indication for full extension of the network that retards the jet velocity, as well as an indication for a substantial mass loss due to evaporation (Fig. 2.10).

The flow regime inside the jet was found to be laminar, with observed streamlines and an almost uniform vertical velocity across the jet (Fig. 2.11).

The polymer concentration mapping along and across the jet makes use of the different X-ray mass absorption coefficients of the polymer and solvent, $\varepsilon_p$ and $\varepsilon_s$, respectively. The absorption coefficient of the polymer solution is given by
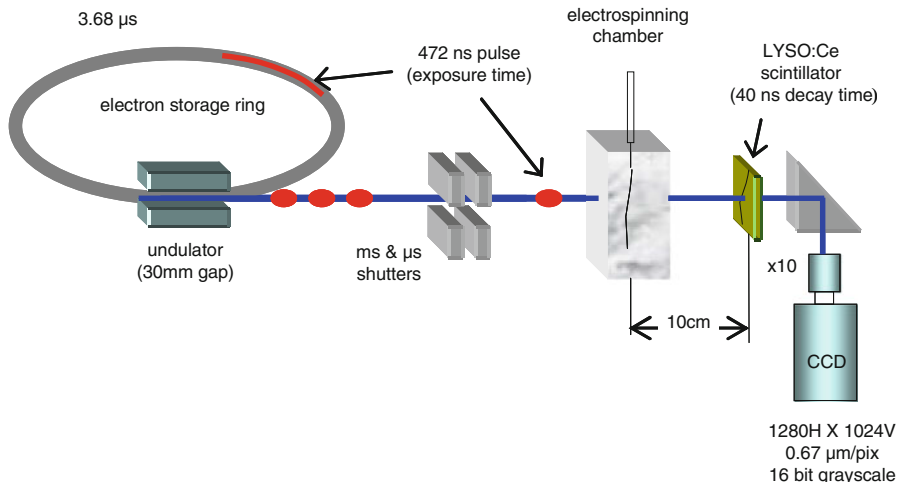


**Fig. 2.8** Experimental setup of X-ray imaging of electrospinning jets. A millisecond shutter was set up in series with a very fast galvano-based shutter that opened the path for less than 100 μs each second. The beam penetrated the jet, and was converted to a digital image by a scintillator. The CCD camera was timed to capture the first released pulse [28]
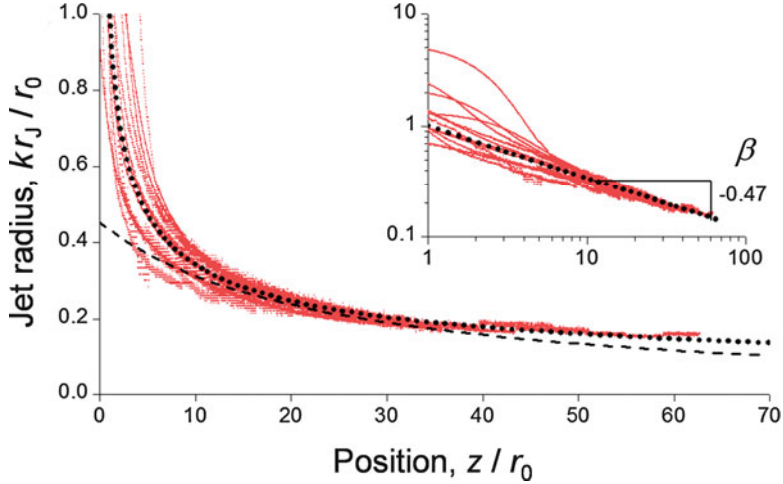
**Fig. 2.9** Normalized jet radius $kr_J/r_0$ at position $z/r_0$ along the jet, for the combined data of 13 electrospinning tests, where each test set was multiplied by the constant $k$ pertaining to that test. The power fit exponent $\beta$ is shown in the *inset*. The measured dimensionless parameter $k$ compares well with the theoretical prediction [28]
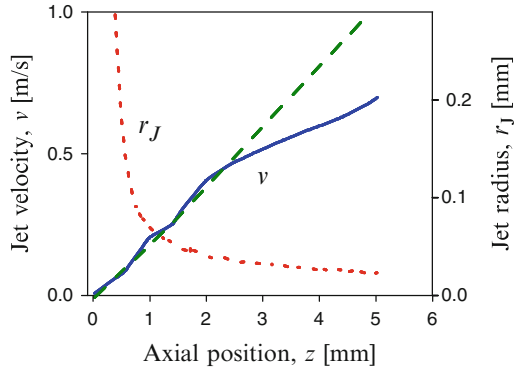


**Fig. 2.10** Example of vertical velocity measurement using silica microbeads (*solid line*), compared to velocity estimation from the measured jet radius $r_J$ assuming mass conservation (*dashed line*). Electrospinning of PEO 5 %, under an electric field of 4 kV/cm, at flow rate of 6.4 mL/h [28]

$\alpha(r,z) = \varepsilon_p c_p(r,z) + \varepsilon_s c_s(r,z)$ [38], where $c_p$ and $c_s$ denote the mass concentrations of the polymer and solvent, respectively, and the coordinates $(r,z)$ are the radial and axial position in the jet, respectively. Thus, the change in the local polymer concentration, $\Delta c_p(r,z)$, is linearly dependent on the change in the local absorption coefficient $\Delta\alpha(r,z)$:

$$\Delta c_p(r,z) = \frac{\Delta\alpha(r,z)\rho_p}{\varepsilon_p\rho_p - \varepsilon_s\rho_s},   \tag{2.11}$$

where and $\rho_p$ and $\rho_s$ are the densities of the polymer and solvent, respectively [28]. $\Delta\alpha(r,z)$ is calculated by comparing the measured X-ray transmission (*exp*) to

**Fig. 2.11** Typical flow
field during electrospinning
of PEO 5 % solution in
water, mixed with 0.9 vol %
silica microbeads, under an
electric field of 4 kV/cm and
flow rate of 6.4 mL/h.
Obtained by two-pulsed
X-ray imaging (73.6 μs time
interval) of a 1 mm-long jet
section [28]
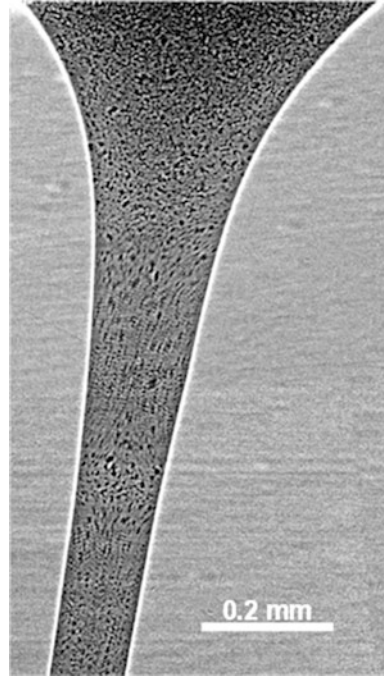


a simulated transmission for a 'still' jet (*sim*), at a given beam travel distance
through the jet $d(r, z)$ [28]:

$$\Delta\alpha(r,z) \cong -\frac{1}{d(r,z)}\ln\left[\frac{T_{\exp}(r,z)}{T_{sim}(r,z)}\right]\left[\frac{\alpha_0}{\alpha_{sim}(r,z)}\right]. \tag{2.12}$$

The correction factor $\alpha_0/\alpha_{sim}$ filters out the effects of scattering in a homogenous jet,
and is used as an approximation for the non-homogenous electrospinning jet.

Concentrations were found to rapidly increase below a critical jet radius of
~25 μm (equivalent to radius reduction ratio of 0.2) (Fig. 2.12), a possible evidence
for full network extension and of rapid evaporation that occurs much earlier than
theoretical predictions found in the literature. When depicted versus the jet radius,
the concentration curves collapse into groups of common initial solution concen-
tration. The concentration crossover occurs at a lower radius for the lower solution
concentration, as predicted in (2.8). The concentration theoretical prediction (2.10),
depicted in the inset of Fig. 2.12, conforms well to the experimental results, hence
favoring the stretching premise over evaporation. These results confirm that the
stretching crossover position depends predominantly on the solution initial concen-
tration, and is invariant with respect to the electrospinning materials and conditions.
Note that the concentration increase is slightly slower in the experiment compared
to the theoretical curve, possibly accounting for the stretching and compacting
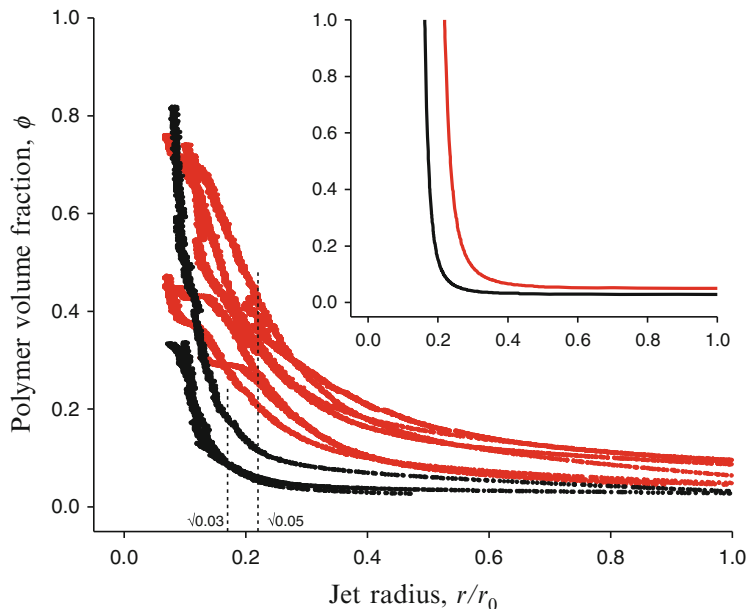retardation caused by the untangling of chains.

**Fig. 2.12** Polymer volume fraction, $\phi_p$, vs relative jet radius, $r_J/r_0$, derived from the X-ray absorption measurements at jet center, for 13 tests of PEO 3 % (*black lines*) and 5 % (*red lines*). The predicted crossover radius from (2.8) is indicated for both solution concentrations at position $\sqrt{\phi}$. The *inset* depicts the corresponding theoretical prediction [28]

Concentration variation across the jet revealed high concentrations at the jet boundary due to evaporation, as well as a concentration rise at the jet center within ~1 mm from the jet start (Fig. 2.13), in agreement with the model and simulation.

Evaporation becomes dominant when stretching is weaker [e.g. at lower electric field and/or higher flow rate – see (2.1) and the definition of $k$], reducing or canceling the concentration peaks measured at the jet center (Fig. 2.14). Such tuning of parameters demonstrates the balance between the effects of evaporation and stretching, which determines the polymer network non-equilibrium conformation during electrospinning, and explains the diversity of macrostructures and properties found in solid nanofibers (see examples in Fig. 2.2). Specifically, dominant stretching is expected to yield uniform structures with axially oriented molecules and better mechanical properties, whereas dominant evaporation may result in porous nonuniform structures.

The technique of X-ray imaging during electrospinning was specifically developed for this research, including the algorithms and methods for processing and analyzing the recorded data. These experiments provided information on internal flow and concentration variations unattainable by other in-situ measurement methods. Fast X-ray phase contrast imaging provides high penetrability at very short exposures, allowing absorption measurements of the unsteady jet, as well as
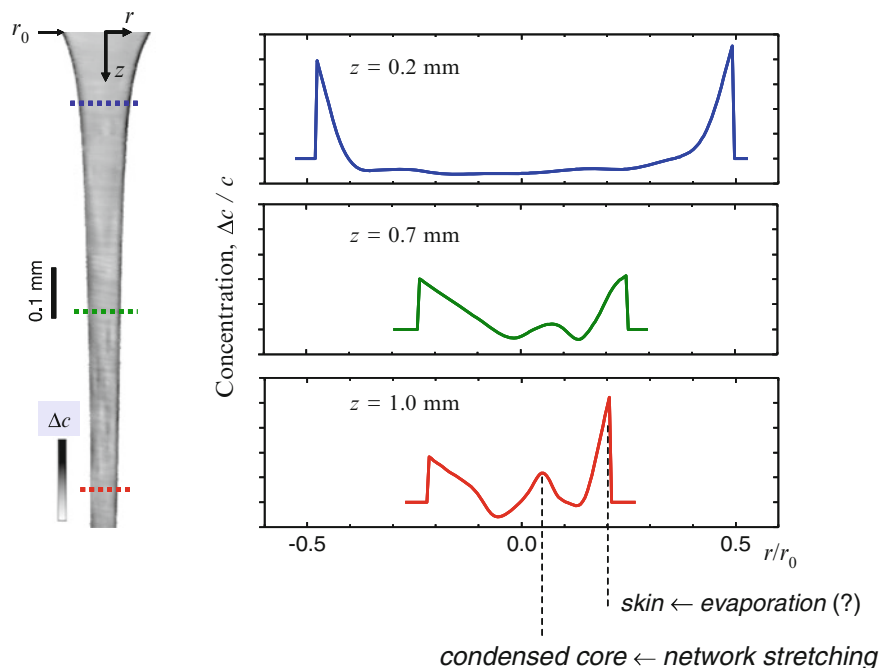
**Fig. 2.13** Typical relative polymer concentration change across the jet, $\Delta c_p/c$, vs the relative radial distance from the jet center, $r/r_0$, for several axial positions $z$ along the jet. The data are derived from X-ray absorption measurements of PEO 5 %, under an electric field of 2.8 kV/cm and flow rate of 1.9 mL/h [28]

enhanced phase boundary contrast, allowing high resolution viewing of the narrow jet and embedded particles.

## 2.4 Entanglement Loss and Short Nanofibers

As already pointed out, the validity of the network modeling is restricted to the initial stage of the jet, where elastic elongation is still possible and the network can be assumed to maintain its degree of entanglement. However, the effects of entanglement loss due to the high strain rate cannot be neglected when considering the final polymer conformation. When carrying out the electrospinning process to its extreme conditions, jet fragmentation (Fig. 2.15) was observed in the appearance of short nanofibers (Fig. 2.16), allowing quantification of the polymer entanglement loss under a high strain rate extensional flow.

Using PMMA of several molar masses, dissolved at different concentrations in solvent blends of varying quality, and tuning the electric field intensities and flow rates, the occurrence of short nanofibers, as well as of beads-on-string, was clearly
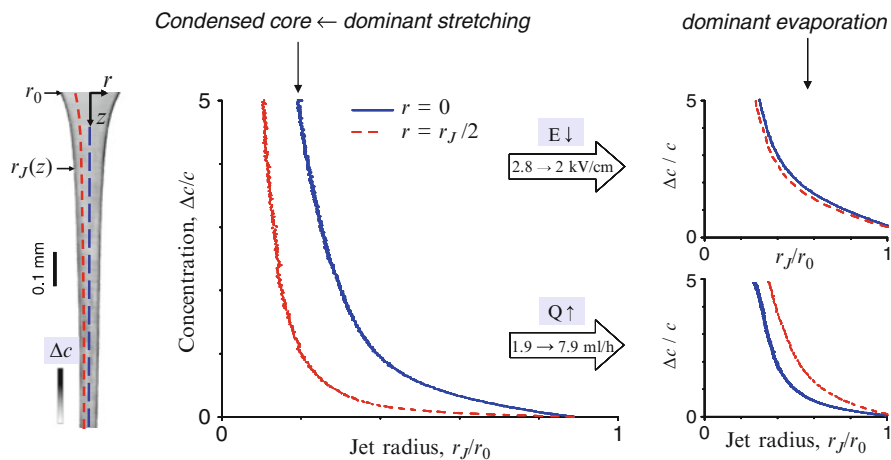
**Fig. 2.14** Comparison of the relative concentration change, $\Delta c_p/c$, at the jet center ($r = 0$) to that measured at a radial offset from the center ($r = r_J/2$), presented vs. the relative jet radius $r_J/r_0$. The data were derived from X-ray absorption measurements of PEO 5 %, with modulation of the flow rate $Q$ and electric field $E$ [28]
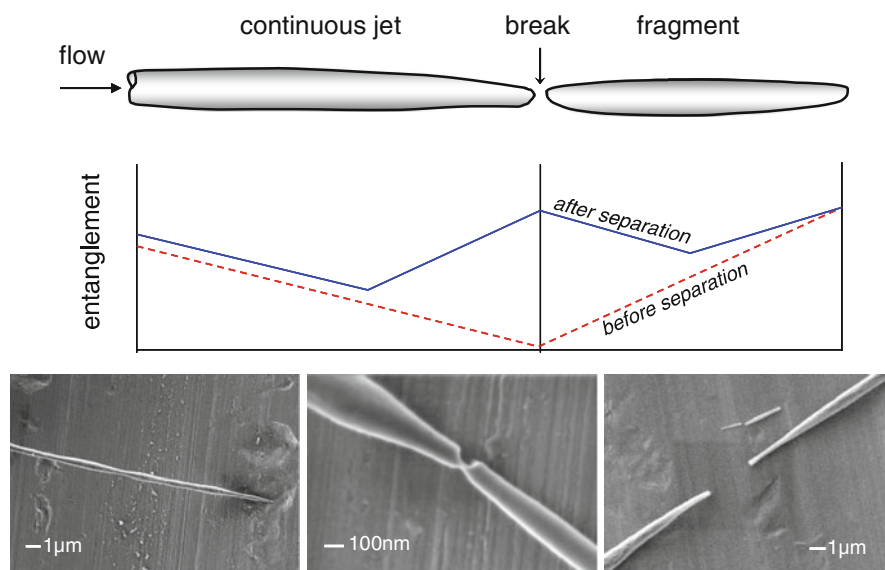


**Fig. 2.15** (*top*) Illustration of jet fragmentation as a result of untangling of the polymer network in low-concentration solutions under high electric fields. (*bottom*) SEM micrographs of the fragmentation of PMMA fibers [29]
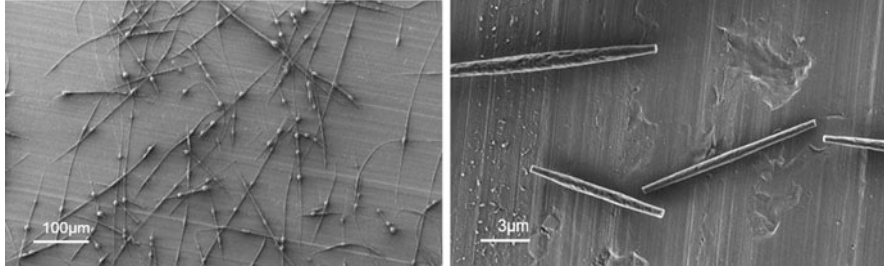
**Fig. 2.16** SEM micrographs of electrospun short PMMA fibers [29]

identified and mapped (Fig. 2.17). Also, the dependence of the short nanofiber length and diameter on the material and process variables was characterized in the form of empirical scaling expressions. Short nanofibers appeared at solution concentrations slightly above the entanglement concentration $\phi_e$, when the electric field intensity was high and the flow rate low. In other words, short nanofibers appeared, and their length was shorter, when the polymer molar mass, concentration, and solvent quality were lower and the flow strain rate was higher. Under such favorable low entanglement and high stretching conditions, the elastic extension of the polymer network accelerates the entanglement loss, eventually leading to separation of the network and fragmentation of the jet.

Using the known jet rheology and the premise of affine extension of the polymer network, a disentanglement model was developed. The underlying assumption is that the entanglement nodes are moving at the same velocity as the jet, while chains are allowed to disentangle but remain highly stretched (Fig. 2.18). Thus,

$$\frac{l}{l_0} \approx \frac{v}{v_0} \approx k^2 \left(\frac{z}{r_0}\right)^{2\beta}, \tag{2.13}$$

where the initial end-to-end distance of a chain section between two entanglements is given by $l_0 \approx b\phi^{-2/3}$ for a $\theta$-solvent [39], and the jet parameter $k$ depends on the material and process parameters (2.1) [29].

The short fibers modeled length for a $\theta$-solvent is given by

$$\frac{L}{r_0} \approx \frac{z_s}{r_0} \approx k_0^{-2} N^{7/2} \phi^{41/9}$$
$$k_0 \cong \varepsilon_m^{1/6} r_0^{2/3} \sigma^{1/4} \eta_s^{-5/12} v_0^{-2/3} E^{5/6}, \tag{2.14}$$

where the semi-dilute solution viscosity was written explicitly [39] as $\eta \approx \eta_s N^3 \phi^{14/3}$ for a $\theta$-solvent [29]. The modeled diameter of short and continuous fibers for a $\theta$-solvent is
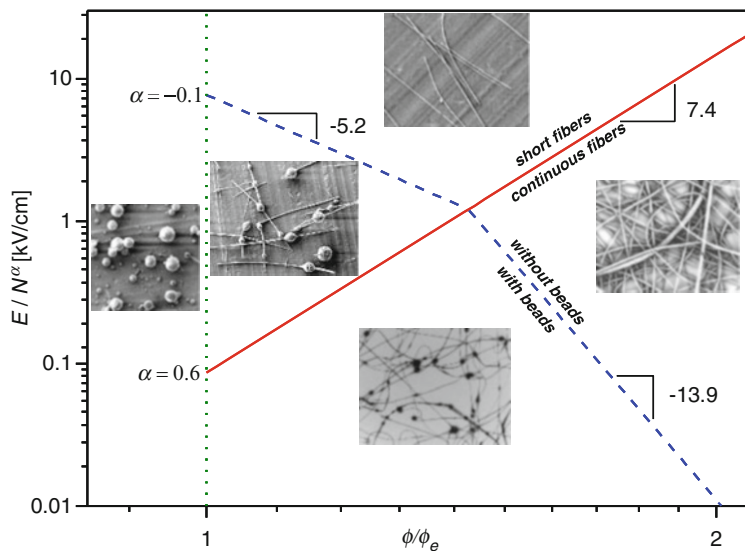
**Fig. 2.17** Electrospun PMMA fibers, short fibers and beads, and measured conditions for their creation, mapped over the electric field $E$, the relative polymer concentration $\phi/\phi_e$, and the degree of polymerization $N$ [29]

**Fig. 2.18** Illustration of polymer untangling during electrospinning, and definition of the modeling parameters. Elastic stretching followed by relaxation of chains gradually disentangle chains from the network. The subscript $s$ denotes the jet break point [29]
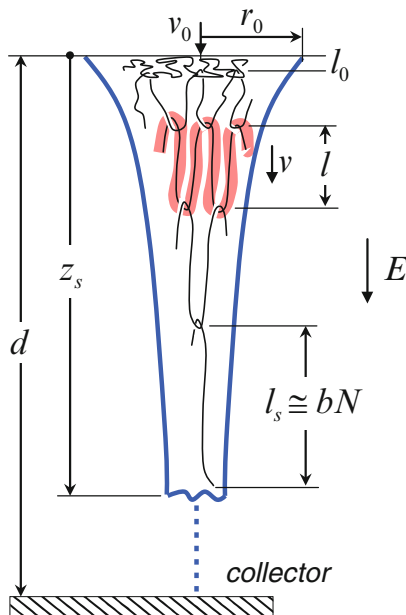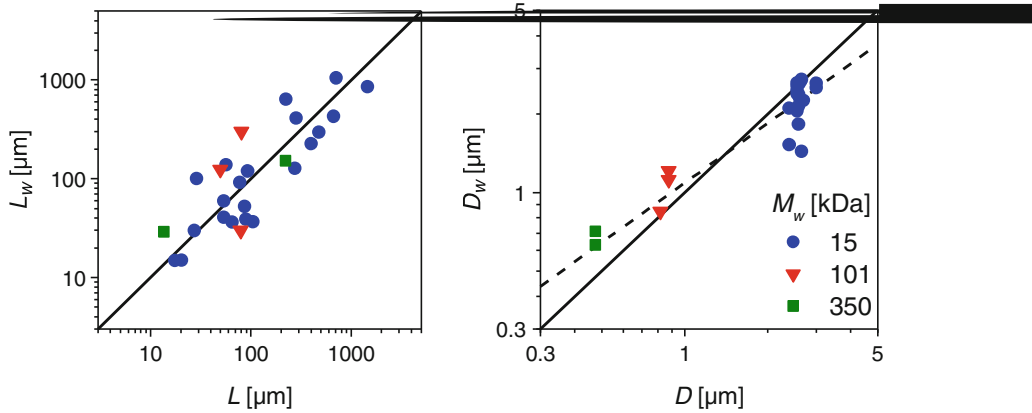
**Fig. 2.19** Experimental and theoretical short nanofibers dimensions. (**a**) Measured length $L_w$ versus the theoretical length $L$. (**b**) Measured diameter $D_w$ versus the theoretical diameter $D$ [29]

$$\frac{D}{r_0} \approx \sqrt{\phi \frac{l_0}{l}} \approx \begin{cases} \phi^{1/6}/N^{1/2} & \text{short fibers} \\ k_0^{-1}(d/r_0)^{-1/2} N^{5/4} \phi^{22/9} & \text{continuous fibers,} \end{cases} \qquad (2.15)$$

where the local condensed polymer diameter is reduced by the extension factor $\sqrt{l/l_0}$ [29]. The experimental results and theoretical predictions for short nanofibers correlate well, confirming the proposed disentanglement mechanism (Fig. 2.19). Diameter measurements of continuous fibers [15, 40] also correlate well with the model.

An important outcome of the analysis is the dependence of the fiber diameter on the material and process parameters (Fig. 2.20). The diameter of short nanofibers grows weakly with increasing the relative concentration, while their length grows sharply. When the concentration is increased beyond a transition point, continuous nanofibers are created and the diameter's growth slope increases abruptly. The transition point identifies the conditions that lead to a minimal possible radius in continuous fibers.

While the diameter of a continuous nanofiber depends on the solution's relative concentration by a power of 2.4, the corresponding power in short nanofibers is only 0.17, marking a distinct difference between the two morphologies. The reason for these differences is that in continuous nanofibers, the process of disentanglement is not carried out until complete separation of the polymer network as in short nanofiber, since it is terminated at the collector, and therefore the amount of entanglement loss, and hence the diameter, depend on the flow dynamics and the electrodes gap size.

The high elastic stretching and entanglement loss required to create short nanofibers are likely to lead to an ordered, aligned solid nanostructure with improved mechanical properties. At the same time, since fragmentation occurs before full solidification, the polymer network may partially relax in solvent rich
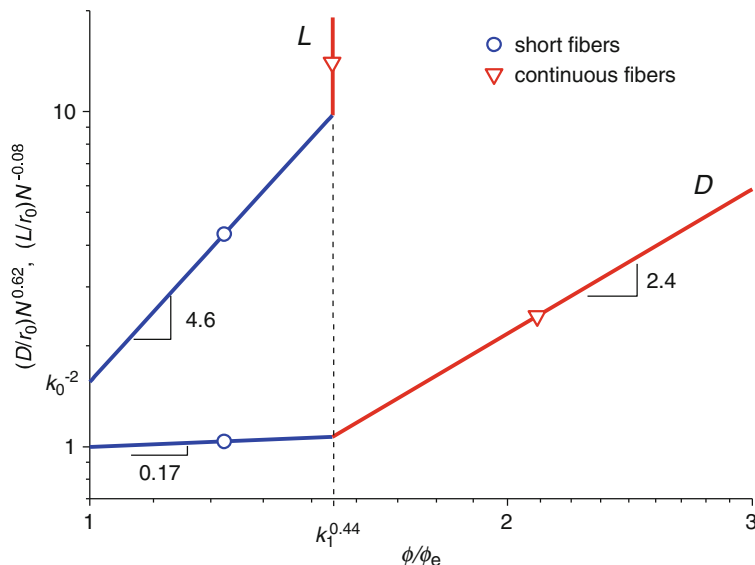
**Fig. 2.20** Nanofiber length $L/r_0$ and diameter $D/r_0$ versus the relative concentration $\phi/\phi_e$. $N$ is the degree of polymerization, $k_1 = k_0\sqrt{d/r_0}$, $d$ is the gap distance between the electrodes, and $r_0$ is the jet initial radius [29]

areas and leave voids in the polymer matrix. Hence, a nonuniform structure can result in both the axial and radial directions, with regions of aligned rigid structure and regions of amorphous porous structure. The prospect of nanofiber size tuning, and hence their morphology, in accordance with the proposed model, can be exploited to improve their as-spun mechanical, optical and thermodynamic properties, such as the elastic modulus and light polarization. Combined with the possible biaxial nonuniform nanostructure, it may find interesting applications in tissue engineering, drug delivery, composites reinforcement, filtration, electrical and thermal conduction, and light amplification.

## 2.5  Fiber Nanostructure and Mechanical Properties

The gradual solidification of the jet during the advanced stage of electrospinning, which results in viscosity increase, crystal growth, and partial relaxation of chains from their non-equilibrium state back toward their coil state, raises a question whether the beneficial outcome of stretching and molecular packing remains in the solid fiber.

The opportunity presented itself in electrospinning of the conjugated polymer MEH-PPV. This optically active, electrically conductive polymer is of high interest because of its potential applications in semi-conducting devices such as field effect

**Fig. 2.21** Simulated ideal
chain conformations of a
conjugated polymer. From
*top*: polymer network at
rest; a single chain with $N$
$= 146$; strands (subchains)
with different defects
concentration, *left* $N_s = 14$
($n = 5$ beads, 10 % defects),
*right* $N_s = 67$ ($n = 3.4$
beads, 15 % defects);
stretched subchains during
electrospinning at distances
of $z = 0.08$ mm and $z = z_s$
$= 0.16$ mm from the jet
exit, $N_s = 14$ [13]
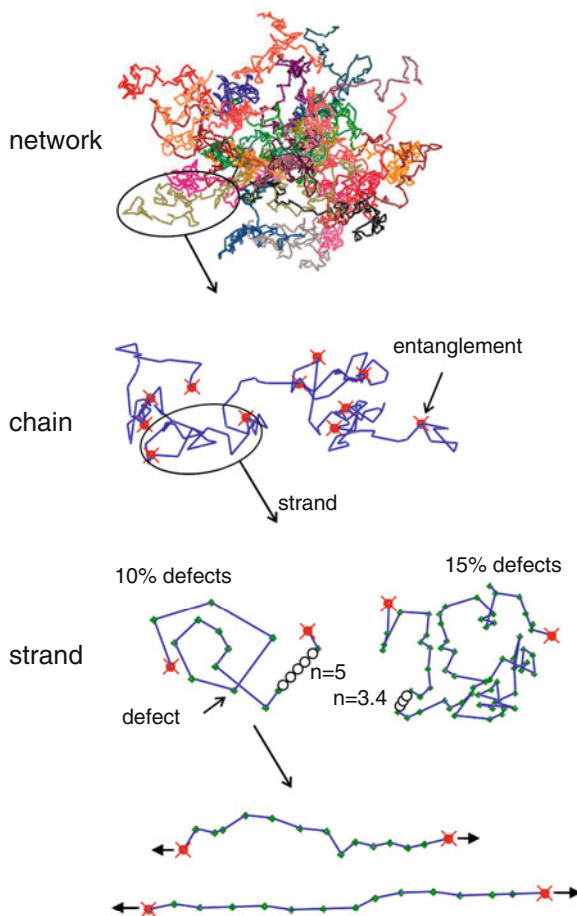
transistors, light emitting diodes, active layer in lasers, and sensors. Two properties
make this polymer an excellent candidate for examining the posed question. First,
MEH-PPV has high absorption in the visible waveband, specifically around the
wavelength of the laser used for radiation, lending itself to optical probing. Second,
unlike freely jointed chains, conjugated polymer chains are not flexible, but are
rather semi-flexible as a result of the high bending rigidity of the chain backbone,
which is composed of alternating single and double covalent bonds. Owing to
inherent bonding defects, which substitute rigid conjugated links by flexible tetra-
hedral links, the conjugated chains can be described as flexible chains having longer
Kuhn (rigid) segments (Fig. 2.21). Consequently, as shown by our generalized
modeling and simulation (more details later), the stretching and lateral contraction
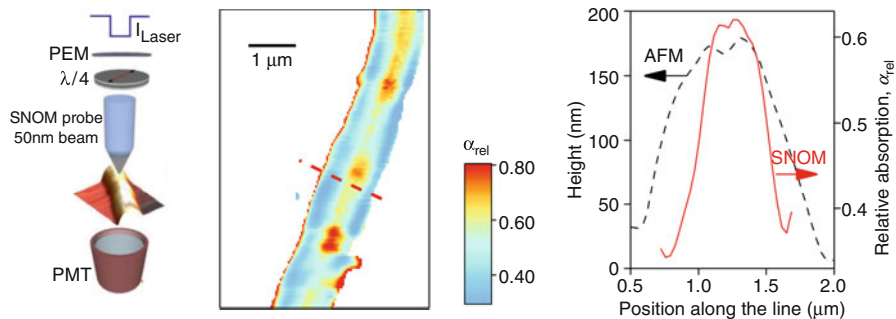phenomena should be more pronounced in this class of polymers.

**Fig. 2.22** SNOM scanning of a single fiber (*left*). SNOM map of the nanoscale variation of the relative optical absorption coefficient of an MEH-PPV electrospun fiber (*center*). Fiber topography (*dashed line*, measured by AFM) and the corresponding relative optical absorption, $\alpha/\alpha_{max}$ (*continuous line*, measured by SNOM) along a transverse line (*right*). The polymer density is proportional to the absorption coefficient [12, 13]



**Fig. 2.23** Young's modulus map measured by AFM indentation at the cross section of an MEH-PPV nanofiber embedded in UV-cured polymer (*red*). The modulus at the fiber core (*blue*) is more than twice the modulus at its boundary (*yellow*) [12]
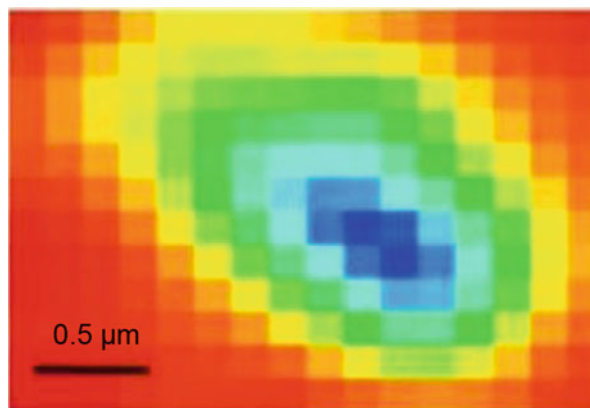
Measurements by high resolution, scanning near-field optical microscopy (SNOM) revealed a core-sheath structure, in which the fiber core has a higher density, whereas closer to the fiber boundary the density is lower (Fig. 2.22).

This observation was strengthened by force-indentation measurements of the elastic modulus at the cross-section of the fiber, using atomic force microscopy (AFM), which showed a higher modulus at the fiber center with respect to the boundary (Fig. 2.23), indicative of higher density and possibly molecular ordering at the core.

These results confirm that the close-packed molecular conformation of the polymer network in the liquid jet, demonstrated by the simulation of the semi-flexible conjugated polymer (Fig. 2.24), is essentially retained in the solid fiber.

In perspective, the found graded-density internal structure can possibly improve charge transport by the fiber core, whereas the lower density sheath can determine the amplification of light guided in the fiber. Similarly, for scaffold applications, the
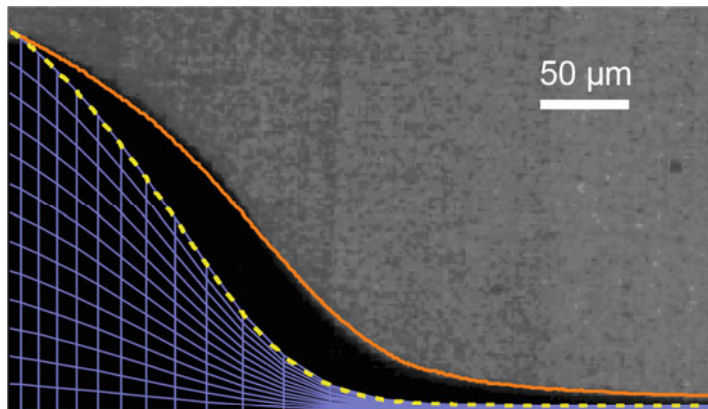
**Fig. 2.24** Simulated polymer network mesh, superimposed on an MEH-PPV electrospinning jet (only the upper half is shown). Viewed mesh density is diluted × 300 in each direction. Conditions: electric field 1.8 kV/cm, flow rate 10 μL/min, polymer volume fraction 0.025 [12]

core can provide the needed strength, rigidity, and conductivity, while the boundary layer has enhanced material absorption and adhesion properties.

## 2.6    Chain Orientation in Fibers

A valid concern is whether the observed dense region at the fiber core consists of an ordered structure or an amorphous structure. In an ordered structure, the mechanical properties of the nanofiber should be improved with respect to bulk material. Moreover, in conjugated polymers such as MEH-PPV, ordering and orientation of chain sections results in a longer effective conjugation length, and consequently longer chromophores (chain parts responsible for color absorption or excitation) and improved optical and electrical properties. We exploited the unique optical properties of conjugated polymers to investigate this concern by measurements of optical absorption and polarization modulation.

The most common process used in producing conjugated polymer macrostructures is spincasting. Electrospinning of conjugated polymers is usually avoided due to their low miscibility, or carried out by mixing other polymers in the solution or by using the core-shell technique. However, while amorphous aggregation of the polymer is favored in films, the elongational dynamics of electrospinning leads to extended structures having interchain alignment. Measurements of the absorption spectra of nanofibers, compared to those of spincast films, showed a peak red shift, which indicates an increase of the effective conjugation length attributable to a more ordered molecular packing. Additionally, the absorption and photoluminescence linear dichroism spectrums, measured on uniaxially aligned MEH-PPV nanofibers, evidence a predominance for light polarized along the fiber longitudinal
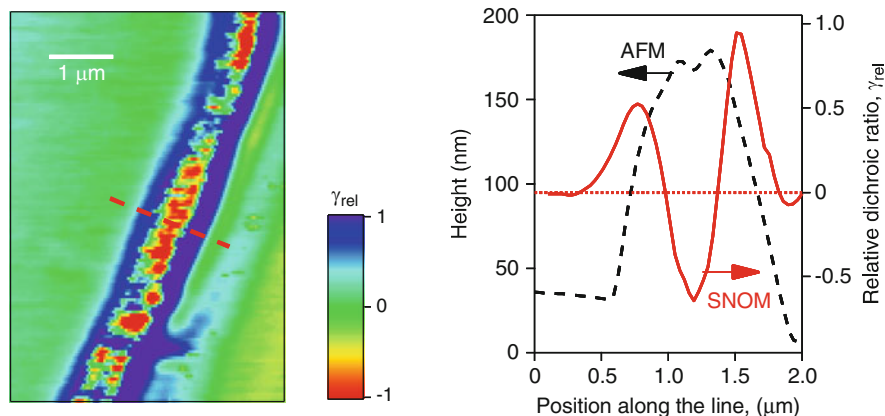
**Fig. 2.25** SNOM map of the nanoscale variation of the relative dichroic ratio of an MEH-PPV electrospun fiber (*left*). Fiber topography (*dashed line*, measured by AFM) and the corresponding relative dichroic ratio, $\gamma/\gamma_{max}$, where $\gamma = (I_{//} - I_{\perp})/(I_{//} + I_{\perp})$ and $I$ is the transmitted intensity (*continuous line*, measured by SNOM with polarization modulation), along a transverse line (*right*). The minimum indicates preferred molecular alignment in the axial direction, while the maxima indicate preferred radial alignment [13]

axis, a fingerprint of a preferential alignment of the polymer backbones along the fiber length.

The nanoscale mapping of the local dichroism of individual fibers, measured by polarized near-field optical microscopy (Fig. 2.25), unveiled for the first time the presence of an internal spatial variation of the molecular order. Specifically, these results confirm the presence of a core (of width ~40 % of fiber diameter) with axially aligned molecules, and a sheath (envelope) with almost radially oriented molecules. The unexpected radial orientational preference in the fiber sheath is attributed to relaxation of polymer chains in the lower density region, combined with crystallic growth in the radial direction.

A key question is how and to what extent the process can be controlled in order to achieve desired nanostructures within the fiber. For that purpose, the polymer network dynamic model and simulation, described in Sect. 2.2, were generalized by tuning the degree of chain flexibility with the segmental aspect ratio (i.e., the number of monomers in a rigid segment, inversely proportional to the bonding defects concentration). Thus, the generalized model applies to a wide range of linear flexible polymers, including conjugated polymers with different bonding defect concentrations, as well as fully flexible polymers that are a particular case of the model in which the segmental aspect ratio is 1.

Given the aspect ratio $n$, polymer volume fraction $\phi$, and solution properties expressed by Flory's exponent $\nu$ and Flory's interaction parameter $\chi$, the number of rigid segments in a single subchain in the polymer network, for a good solvent, is

$$N_s \approx \left(\frac{n}{1-2\chi}\right)^{3(2\nu-1)/(3\nu-1)} \left(n^2\phi\right)^{-1/(3\nu-1)}, \qquad (2.16)$$

and the corresponding correlation length is $\xi \approx b[(1-2\chi)/n]^{2\nu-1}N_s^\nu$ [13]. The exponent $\nu$ is 0.5 for ideal chains, corresponding to $\theta$-solvents, and ~0.6 for real chains, corresponding to good and athermal solvents. Note that when $n = 1$, the equation converges to the classic expression for fully flexible chains, corresponding to the polymer network mesh size.

When the aspect ratio is larger (lower defects concentration), the subchains become shorter and more rigid, in other words the network mesh size is smaller (Fig. 2.26a); specifically, the number of subchain segments is reduced by a power of 4 of the aspect ratio (ideal chain). At concentrations above the athermal limit at point B, the chain conformation is always ideal ($\theta$-solvent condition). When the polymer volume fraction is sufficiently high, subchains start to interact within a single correlation volume, a condition not existing in fully flexible chains, thereby enhancing the likelihood of nematic ordering and molecular orientation (Fig. 2.26b).

The results of the model and simulation for a representative conjugated polymer (10 % defects concentration) are presented in Fig. 2.27, and typical free and extended chain conformations are depicted in Fig. 2.21, exhibiting a similar behavior as in fully flexible chains (Fig. 2.4), but with a strong dependence on the aspect ratio.

Full extension is approached when $\xi_{||} \approx bN_s$, i.e. at the axial position $z_S$ and a corresponding jet radius $r_S$. Using (2.8) and (2.16), the jet radius reduction ratio at full stretching is expressed for good solvents by [13]:

$$\frac{r_0}{r_S} \approx \left(\frac{bN_s}{\xi_0}\right)^{1/2} \approx \left(\frac{n}{1-2\chi}\right)^{(2\nu-1)/(3\nu-1)} \left(n^2\phi\right)^{-(1-\nu)/[2(3\nu-1)]}. \qquad (2.17)$$

Thus, $r_0/r_S$ is reduced as the chain is stiffer (larger $n$), and the exponent of $n$ is $-1$ for a $\theta$-solvent ($\nu = 0.5$) and $-0.25$ for good and athermal solvents ($\nu \cong 0.6$). Note that when $n = 1$ and $\nu = 0.5$, the equation converges to the expression for fully flexible chains in (2.8).

The axial position of full stretching can be obtained by substituting the radius reduction ratio into (2.1), and using the known viscosity expressions for semi-dilute solutions, $\eta \approx \eta_s N^3 \phi^{3/(3\nu-1)}$ for an athermal solvent and $\eta \approx \eta_s N^3 \phi^{14/3}$ for a $\theta$-solvent. Omitting the effect of $n$, the position scales as [13]:

$$\frac{z_s}{r_0} \sim N^{3/2} \begin{cases} \phi^{\frac{\nu+2}{2(3\nu-1)}} & \text{athermal solvent} \\ \phi^{11/6} & \theta\text{-solvent.} \end{cases} \qquad (2.18)$$

In this calculation the approximate value of $k$ was used. The exponent of $\phi$ for the athermal solvent is approximately 13/8. Thus, the model predicts that full extension
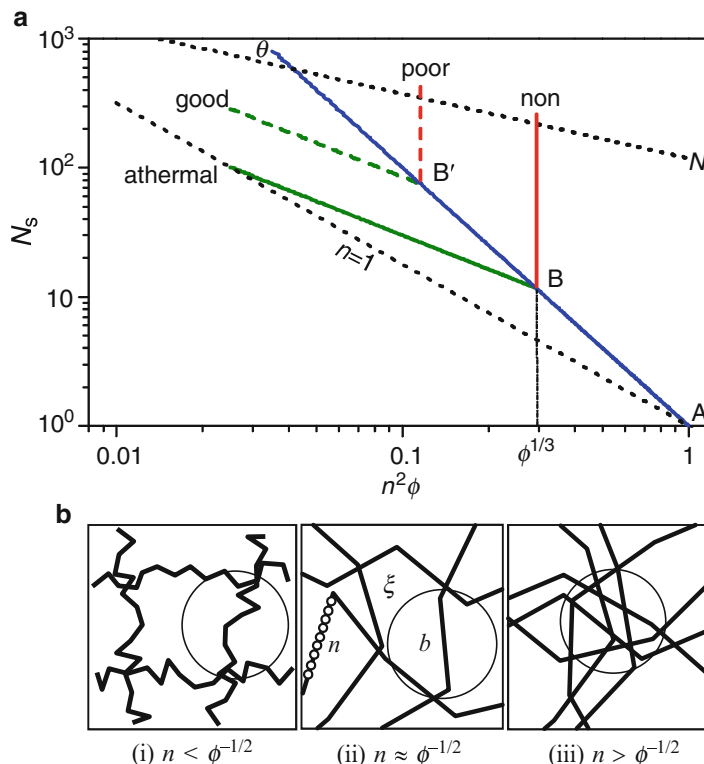
**Fig. 2.26** Conjugated polymer conformation in a solution. (**a**) The number of subchain segments, $N_s$, versus the polymer volume fraction, $\phi$, and the number of beads per segment, $n$, for different solvent quality grades. The *dotted lines* constitute the upper and lower limits for $\phi = 0.025$. Polymer molecular weight is 380 kDa, equivalent to $N_{beads} = 730$. Point B' is depicted for Flory's interaction parameter $\chi \cong 0.38$. (**b**) Crossover [Point A in (**a**)] of the polymer network conformation with respect to the scale of the correlation length $\xi$ (*circles*) and the segment length $b$: (i) regular semi-dilute, $\xi > b$, (ii) crossover, $\xi \approx b$, and (iii) different chains intermix within a single correlation volume, $\xi \approx b$ [13]

of the network occurs at an earlier stage of the jet (closer to the orifice) when the concentration, molar mass, and solvent quality are lower, accounting for lower network entanglement (Fig. 2.28).

Under favorable stretching conditions that expedite full network extension, it is more likely that the extended conformation, and the associated axial molecular alignment, will partially remain in the polymer structure after solidification. Indeed, the measured far-field, macroscale emission from MEH-PPV nanofibers was found to be polarized along the longitudinal axis of the nanostructures, with a degree of polarization dependent on process variables. Specifically, the photoluminescence polarization ratio was raised up to five times that of amorphous polymer, by gradually decreasing the solution concentration down to a volume fraction of
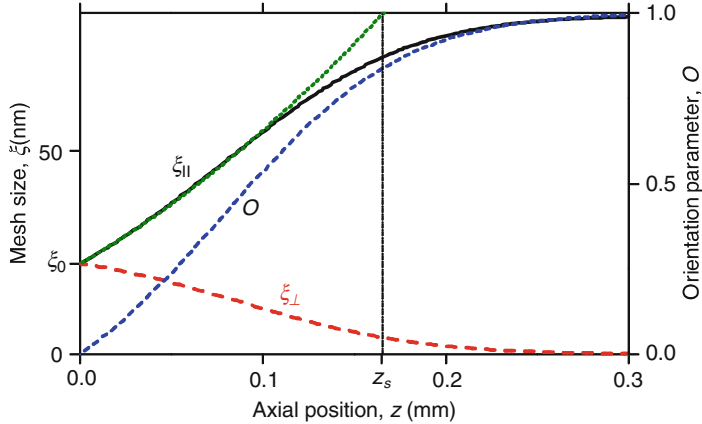
**Fig. 2.27** Simulated subchain length during electrospinning. The axial mesh size $\xi_{\parallel}$, radial mesh size $\xi_{\perp}$, and orientation parameter $O$ are plotted versus the axial position $z$ along the jet. The simulated $\xi_{\parallel}$ (*solid line*) is compared with the theoretical model (*dotted line*). The position close to full subchain extension is designated by $z_s$. Parameters used: ideal chain, $\phi = 0.025$, $n = 5$ beads, bead size $d = 1.2$ nm, $\xi_0 \cong 20$ nm, $N_s = 14$ segments. Jet dynamics is derived from Fig. 2.24 [13]
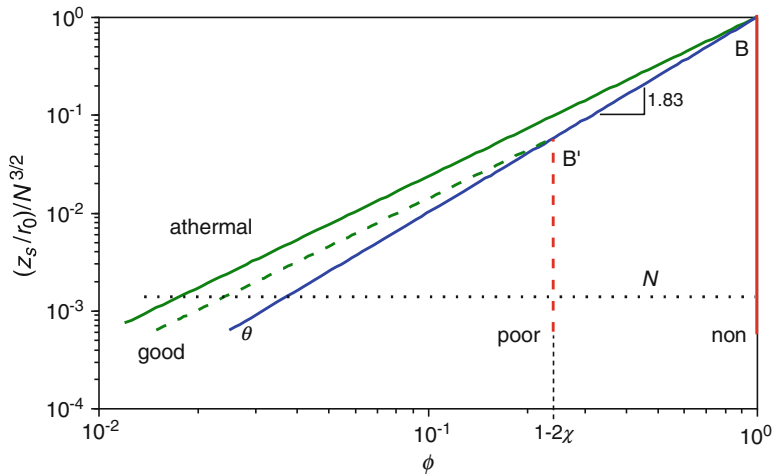


**Fig. 2.28** Axial position where subchains approach full extension, $z_s/r_0$, normalized by $N^{3/2}$ ($N$ is the chain's number of segments), versus the polymer volume fraction $\phi$ and solvent quality. Modeled for full chain flexibility ($n = 1$). The *dotted line* constitutes the lower limit imposed by $N_s < N$. Prefactors are omitted, and all other influencing parameters (e.g. electric field and flow rate) are assumed constant. Points B and B' are explained in Fig. 2.26 [13]

0.03 (Fig. 2.29), a clear indication for the inverse dependence of the longitudinal molecular alignment on concentration. Thus, the confirmed model provides tools for tailoring of the photophysical properties of the fibers.

**Fig. 2.29** Polarization ratio of an MEH-PPV fiber versus the solution volume fraction, $\phi$. An unpolarized sample (sprayed film) has a polarization ratio of 1, whereas values above 1 indicate a preferred molecular alignment along the axial direction [13]
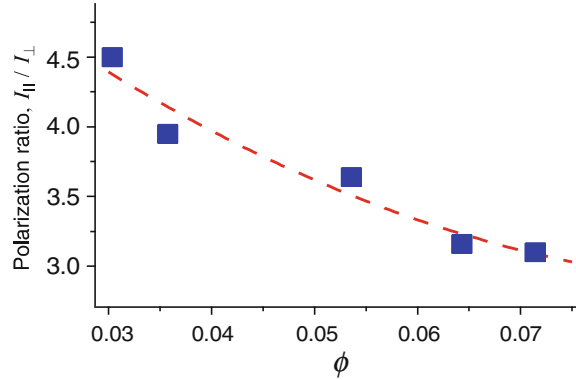


## 2.7  Controlling the Nanostructure

This research focused on the analysis of the polymer matrix evolution during a strong extensional flow of a polymer solution, using the technique of electrospinning as a test bed. When stretching is dominant, the structures revealed in electrospun nanofibers are dense, stiff and ordered, with a preference for molecular alignment along the fiber longitudinal axis. The observed structure is anisotropic, with a core-sheath conformation that can be utilized for improving charge transport, light amplification, and scaffolding (Fig. 2.30).

The study shows how the nanofiber diameter can be tuned by modifying the electrospinning conditions. The diameter can be decreased to the point just before fragmentation, resulting in the smallest achievable fiber diameter in given conditions, and potentially yielding the highest mechanical properties possible for these conditions, as well as enhanced electrical and optical properties.

The size dependence of these properties, well-documented by numerous experiments, is the consequence of the fiber nanostructure, namely the level of polymer entanglement and the degree of orientation in the solid structure, as well as the existence of super-molecular structures created by correlation between aligned molecules. It can be shown that these properties and the diameter are strongly related by

$$D \sim \left( \frac{n_{\text{ent}}}{\langle \cos\theta \rangle} \right)^{1/2}, \tag{2.19}$$

where $n_{\text{ent}}$ is the number density of entanglements and $\langle \cos\theta \rangle$ is the average molecular orientation. This relationship is illustrated in Fig. 2.31.

In conclusion, the nanostructure of electrospun fibers can be controlled by tuning the material and process properties, such as the polymer type and molar mass, solvent quality, solution concentration, injection velocity and diameter, intensity of the electric potential, and the electrodes gap distance. Specific fiber properties can
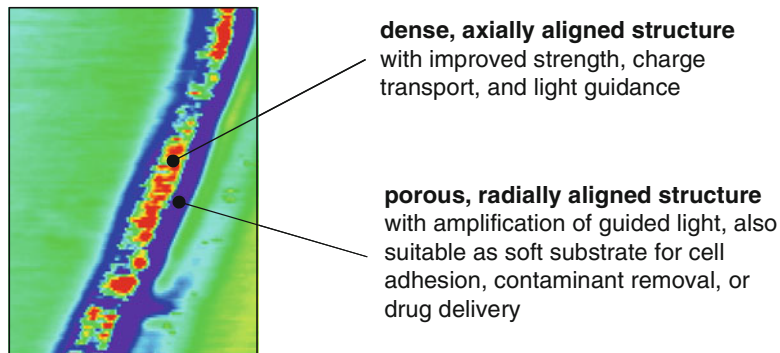
**dense, axially aligned structure**
with improved strength, charge transport, and light guidance

**porous, radially aligned structure**
with amplification of guided light, also suitable as soft substrate for cell adhesion, contaminant removal, or drug delivery

**Fig. 2.30** Core-sheath anisotropic structure revealed in electrospun MEH-PPV fibers [13]
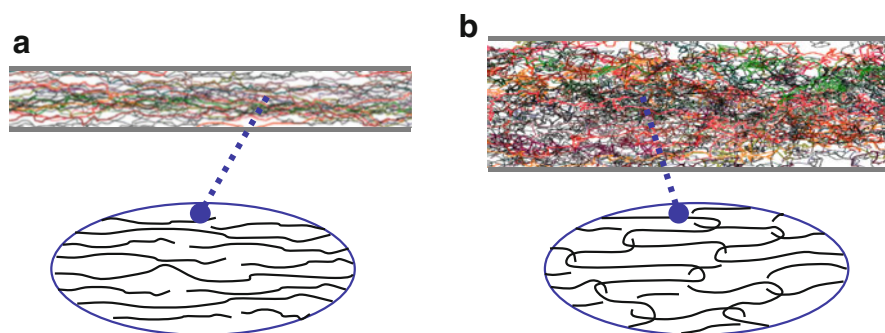


**Fig. 2.31** Illustration of possible molecular structures in electrospun nanofibers. (**a**) Small fiber diameter with highly aligned untangled chains, typical of short nanofibers. (**b**) Large fiber diameter with partially aligned and partially entangled chains, typical of continuous nanofibers

be manipulated and tailored by making use of the trends learnt from the modeling and experimental characterization.

# References

1. A.L. Andrady, *Science and Technology of Polymer Nanofibers* (Wiley, Hoboken, 2008)
2. J. Stanger, N. Tucker, M. Staiger, *Electrospinning*. Rapra Rev. Rep. **16**(10) (2005)
3. Z.M. Huang, Y.Z. Zhang, M. Kotaki, S. Ramakrishna, A review on polymer nanofibers by electrospinning and their applications in nanocomposites. Compos. Sci. Technol. **63**(15), 2223–2253 (2003). doi:10.1016/S0266-3538(03)00178-7

4. I.U.G. Gogotsi, *Nanotubes and Nanofibers*. Advanced materials series (CRC Taylor & Francis, Boca Raton, 2006)
5. M. Burman, A. Arinstein, E. Zussman, Do surface effects explain the unique elasticity of polymer nanofibers? Europhys. Lett. **96**, 16006 (2011)
6. Y. Liu, S. Chen, E. Zussman, C.S. Korach, W. Zhao, M. Rafailovich, Diameter-dependent modulus and melting behavior in electrospun semicrystalline polymer fibers. Macromolecules **44**(11), 4439–4444 (2011). doi:10.1021/ma200262z
7. Y. Ji, C. Li, G. Wang, J. Koo, S. Ge, B. Li, J. Jiang, B. Herzberg, T. Klein, S. Chen, J.C. Sokolov, M.H. Rafailovich, Confinement-induced super strong PS/MWNT composite nanofibers. Europhys. Lett. **84**(5), 56002 (2008). doi:Artn 56002 doi:10.1209/0295-5075/84/56002
8. M. Burman, A. Arinstein, E. Zussman, Free flight of an oscillated string pendulum as a tool for the mechanical characterization of an individual polymer nanofiber. Appl. Phys. Lett. **93**(19), 193118 (2008). doi:Artn 193118 doi:10.1063/1.3000016
9. A. Arinstein, M. Burman, O. Gendelman, E. Zussman, Effect of supramolecular structure on polymer nanofibre elasticity. Nat. Nanotechnol. **2**(1), 59–62 (2007). doi:10.1038/nnano.2006.172
10. X.M. Sui, H.D. Wagner, Tough nanocomposites: the role of carbon nanotube type. Nano Lett. **9**(4), 1423–1426 (2009). doi:10.1021/Nl803241y
11. X.M. Sui, E. Wiesel, H.D. Wagner, Enhanced mechanical properties of electrospun nanofibers through NaCl mediation. J. Nanosci. Nanotechnol. **11**(9), 7931–7936 (2011). doi:10.1166/jnn.2011.4760
12. A. Camposeo, I. Greenfeld, F. Tantussi, S. Pagliara, M. Moffa, F. Fuso, M. Allegrini, E. Zussman, D. Pisignano, Local mechanical properties of electrospun fibers correlate to their internal nanostructure. Nano Lett. **13**(11), 5056–5062 (2013). doi:10.1021/Nl4033439
13. A. Camposeo, I. Greenfeld, F. Tantussi, M. Moffa, F. Fuso, M. Allegrini, E. Zussman, D. Pisignano, Conformational evolution of elongated polymer solutions tailors the polarization of light-emission from organic nanofibers. Macromolecules **47**(14), 4704–4710 (2014). doi:http://dx.doi.org/10.1021/ma500390v
14. T. Han, A.L. Yarin, D.H. Reneker, Viscoelastic electrospun jets: initial stresses and elongational rheometry. Polymer **49**(6), 1651–1658 (2008). doi:10.1016/j.polymer.2008.01.035
15. P. Gupta, C. Elkins, T.E. Long, G.L. Wilkes, Electrospinning of linear homopolymers of poly(methyl methacrylate): exploring relationships between fiber formation, viscosity, molecular weight and concentration in a good solvent. Polymer **46**(13), 4799–4810 (2005). doi:10.1016/j.polymer.2005.04.021
16. D.H. Reneker, A.L. Yarin, E. Zussman, H. Xu, Electrospinning of nanofibers from polymer solutions and melts. Adv. Appl. Mech. **41**, 43–195 (2007). doi:10.1016/S0065-2156(06)41002-4
17. D.H. Reneker, A.L. Yarin, H. Fong, S. Koombhongse, Bending instability of electrically charged liquid jets of polymer solutions in electrospinning. J. Appl. Phys. **87**(9), 4531–4547 (2000)
18. L.M. Bellan, H.G. Craighead, J.P. Hinestroza, Direct measurement of fluid velocity in an electrospinning jet using particle image velocimetry. J. Appl. Phys. **102**(9), 094308 (2007). doi:Artn 094308 doi:10.1063/1.2799059
19. M.M. Hohman, M. Shin, G. Rutledge, M.P. Brenner, Electrospinning and electrically forced jets. I. Stability theory. Phys. Fluids **13**(8), 2201–2220 (2001)
20. Y.M. Shin, M.M. Hohman, M.P. Brenner, G.C. Rutledge, Experimental characterization of electrospinning: the electrically forced jet and instabilities. Polymer **42**(25), 9955–9967 (2001)
21. I. Greenfeld, A. Arinstein, K. Fezzaa, M.H. Rafailovich, E. Zussman, Polymer dynamics in semidilute solution during electrospinning: a simple model and experimental observations. Phys. Rev. E **84**(4), 041806 (2011). doi:Artn 041806 doi:10.1103/Physreve.84.041806

22. E. Zussman, A. Arinstein, Electrospun polymer nanofibers: mechanical and thermodynamic perspectives. J. Polym. Sci. Part B Polym. Phys. **49**(10), 691–707 (2011). doi:10.1002/polb. 22247

23. A.J. Guenthner, S. Khombhongse, W.X. Liu, P. Dayal, D.H. Reneker, T. Kyu, Dynamics of hollow nanofiber formation during solidification subjected to solvent evaporation. Macromol. Theory Simul. **15**(1), 87–93 (2006). doi:10.1002/mats.200500034

24. P. Dayal, T. Kyu, Dynamics and morphology development in electrospun fibers driven by concentration sweeps. Phys. Fluids **19**(10), 107106 (2007). doi:Artn 107106 doi:10.1063/1. 2800277

25. P. Dayal, J. Liu, S. Kumar, T. Kyu, Experimental and theoretical investigations of porous structure formation in electrospun fibers. Macromolecules **40**(21), 7689–7694 (2007). doi:10. 1021/Ma0714181

26. S. Koombhongse, W.X. Liu, D.H. Reneker, Flat polymer ribbons and other shapes by electrospinning. J. Polym. Sci. Part B Polym. Phys. **39**(21), 2598–2606 (2001)

27. C.L. Casper, J.S. Stephens, N.G. Tassi, D.B. Chase, J.F. Rabolt, Controlling surface morphology of electrospun polystyrene fibers: effect of humidity and molecular weight in the electrospinning process. Macromolecules **37**(2), 573–578 (2004). doi:10.1021/Ma0351975

28. I. Greenfeld, K. Fezzaa, M.H. Rafailovich, E. Zussman, Fast X-ray phase-contrast imaging of electrospinning polymer jets: measurements of radius, velocity, and concentration. Macromolecules **45**(8), 3616–3626 (2012). doi:10.1021/Ma300237j

29. I. Greenfeld, E. Zussman, Polymer entanglement loss in extensional flow: evidence from electrospun short nanofibers. J. Polym. Sci. Part B Polym. Phys. **51**(18), 1377–1391 (2013). doi:10.1002/polb.23345

30. I. Greenfeld, Polymer network dynamics during electrospinning and its effect on the fibers nanostructure: Modeling, simulation and experiments. Mechanical Engineering. PhD thesis, Technion, Haifa, 2013

31. V.N. Kirichenko, I.V. Petrianovsokolov, N.N. Suprun, A.A. Shutov, Asymptotic radius of slightly conducting liquid jet in an electric-field. Dokl. Akad. Nauk SSSR **289**(4), 817–820 (1986)

32. A.F. Spivak, Y.A. Dzenis, Asymptotic decay of radius of a weakly conductive viscous jet in an external electric field. Appl. Phys. Lett. **73**(21), 3067–3069 (1998)

33. M.M. Hohman, M. Shin, G. Rutledge, M.P. Brenner, Electrospinning and electrically forced jets. II. Applications. Phys. Fluids **13**(8), 2221–2236 (2001)

34. F.J. Higuera, Stationary viscosity-dominated electrified capillary jets. J. Fluid Mech. **558**, 143–152 (2006). doi:10.1017/S0022112006000024

35. S.N. Reznik, E. Zussman, Capillary-dominated electrified jets of a viscous leaky dielectric liquid. Phys. Rev. E. **81**(2), 026313 (2010). doi:Artn 026313 doi:10.1103/Physreve.81.026313

36. P.G. de Gennes, Coil-stretch transition of dilute flexible polymers under ultrahigh velocity-gradients. J. Chem. Phys. **60**(12), 5030–5042 (1974)

37. P.G. de Gennes, *Scaling Concepts in Polymer Physics* (Cornell University Press, Ithaca, 1979)

38. R.J. Roe, *Methods of X-ray and Neutron Scattering in Polymer Science*. Topics in polymer science (Oxford University Press, New York, 2000)

39. M. Rubinstein, R.H. Colby, *Polymer Physics* (Oxford University Press, Oxford/New York, 2003)

40. M.G. McKee, G.L. Wilkes, R.H. Colby, T.E. Long, Correlations of solution rheology with electrospun fiber formation of linear and branched polyesters. Macromolecules **37**(5), 1760–1767 (2004). doi:10.1021/Ma035689h